Precision wormlike nanoadjuvant governs potency of vaccination

Sun, Z.; Qiao, D.; Shi, Y.; Barz, M.; Liu, L.; Chen, Y.

NANO LETTERS

pubs.acs.org/NanoLett Letter

Precision Wormlike Nanoadjuvant Governs Potency of Vaccination

Ziyang Sun, Dongdong Qiao, Yi Shi, Matthias Barz, Lixin Liu,* and Yongming Chen*

Cite This: *Nano Lett.* 2021, 21, 7236−7243 Read Online

ACCESS | Metrics & More | Article Recommendations | Supporting Information

ABSTRACT: It remains unclear how the precise length of one-dimensional nanovehicles influences the characters of vaccination. Here, a unimolecular nanovehicle with tailored size and aspect ratio (AR) is applied to deliver CpG oligodeoxynucleotide, a Toll-like receptor (TLR) 9 agonist, as an adjuvant of recombinant hepatitis B virus surface antigen (rHBsAg), for treating chronic hepatitis B (CHB). Cationic nanovehicles with fixed width (ca. 45 nm) but varied length (46 nm−180 nm), AR from 1 to 4, are prepared through controlled polymerization and are loaded with CpG by electrostatic interaction. We reveal that the nanoadjuvant with AR = 2 shows the highest retention in proximal lymph nodes. Importantly, it is more easily internalized into antigen-presenting cells and accumulates in the late endosome, where TLR9 is located. Such a nanoadjuvant exhibits the strongest immune response with rHBsAg to clear the hepatitis B virus in the CHB mouse model, showing that the AR of nanovehicles governs the efficiency of vaccination.

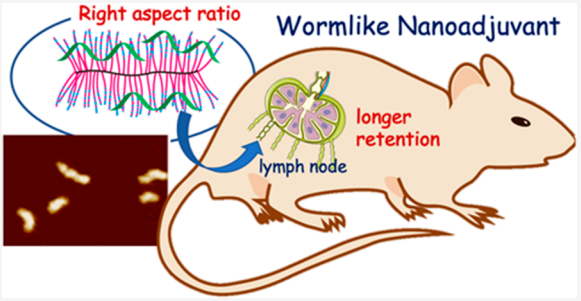

KEYWORDS: *Chronic hepatitis B, Lymph node targeting, Molecular bottlebrush, Nanoadjuvant, Nanovaccine*

INTRODUCTION

Vaccination is a powerful way to combat diseases by engaging with the powerful machinery of the immune system. For a potent vaccine to activate naive lymphocytes, it needs antigens and adjuvants that can activate the innate immunity.[1,2] Lymph nodes (LNs) are central organs of the immune response and enriched with abundant immune cells such as dendritic cells (DCs), macrophages, T-cells, and B-cells.[3,4] Just because of this, LN-targeted delivery of vaccine is becoming an important strategy to enhance immunogenicity. Moreover, immune-stimulatory molecules have been increasingly applied as adjuvants to enhance the efficacy of vaccines. However, due to low molar mass, molecular adjuvants suffer from degradation and nonspecific biodistribution, leading to low bioavailability and systemic inflammatory toxicity.[5] For example, CpG oligodeoxynucleotide (CpG) and tumor necrosis factor-α (TNF-α) would be rapidly degraded by enzymes or expelled from the body to reduce their immune-activating potency.[6,7] By encapsulation into a carrier to form a particulate adjuvant, degradation of molecular adjuvants is inhibited, and meanwhile, nanosized adjuvants can be designed to enhance LN targeting and internalization by immune cells, resulting in substantially enhanced immune stimulation.[8,9]

Physical properties of delivery vehicles, such as size, surface charge, and shape, greatly influence plasma circulation and tumor accumulation as well as cellular uptake.[10] The size of nanoparticles affects the efficiency of their transportation to LNs and localization in LNs substructures, thus finally leading to immune activation pathways.[3,11,12] Furthermore, the shape of nanoparticles could be critical for activating immunity.[13,14] However, few investigations on one-dimensional (1D) nanoparticles, like carbon nanotubes,[15] aluminum oxyhydroxide nanorods,[16] and stretch-formed rods,[17,18] in vaccine application can be found. These 1D particles are rigid and difficult to precisely tune in length. Furthermore, relative to spherical nanoparticles, semiflexible wormlike nanoparticles could exhibit unique characteristics in crossing lymphatic endothelial cells and penetrating the extracellular matrix (ECM) inside LNs to reach immune cells in transportation. However, to our knowledge, precision semiflexible nanovehicles with fixed width but varied length, *i.e.*, with tunable aspect ratio (AR), in a size range needed for LNs targeting (20−50 nm) for a potent vaccination has never been reported. Molecular bottlebrushes (MBBs) with polymer side chains densely grafted along a linear polymeric backbone are unimolecular polymeric nanoparticles, and their AR can be simply tailored by controlling the degree of polymerization (DP) of the backbone and side chains.[19−21] Moreover, because of their polymeric nature, MBBs adopt a semiflexible wormlike shape[22] and may outperform rigid rods in tissue penetration. Because their morphology is stable against disassociation, MBBs are ideal vehicles for mechanism studies on shape effects on the

Received: June 11, 2021
Revised: August 25, 2021
Published: August 30, 2021

https://doi.org/10.1021/acs.nanolett.1c02274
Nano Lett. 2021, 21, 7236−7243

performance of nanovaccines associated with lymph trafficking and immune activation.

Herein, we explore the AR-dependent immune stimulation of semiflexible 1D nanoadjuvants on protective immunization against chronic hepatitis B (CHB), a persistent liver infection caused by hepatitis B virus (HBV), which remains a major global health burden. Tailor-made MBBs of different ARs loaded with CpG were applied as nanoadjuvants, allowing us not only to understand AR-dependent LN and immune cell targeting but also to evaluate the AR-dependent efficiency of immunization combining nanoadjuvant with recombinant hepatitis B virus surface antigen (rHBsAg) to combat CHB (Figure 1).

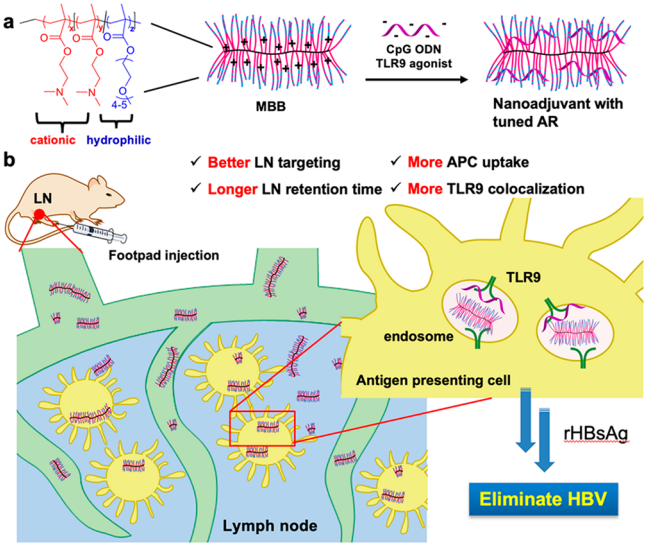

Figure 1. MBBs with defined AR are used to deliver CpG for clarifying AR-dependent LN targeting and immunostimulatory effects in CHB. (a) Cationic MBBs with tuned AR and loaded with anionic CpG by electrostatic interactions. (b) Nanoadjuvants with specific AR combined with rHBsAg show better LN targeting, internalization by resident immune cells, and colocalization with TLR9 following footpad injection, leading to the best performance for clearance of HBV.

RESULTS AND DISCUSSION

Preparation and Characterization of Nanoadjuvants.

To carry the anionic adjuvant CpG, cationic MBBs (Figure 1a) were designed and prepared by controlled polymerization as described in Figure S1. The AR of MBBs is governed by the ratio of backbone to side chain length, and thus, we prepared the backbones with DP of 55, 186, and 590. The backbones, of which every repeating unit contained initiating groups, were then applied as macroinitiators to graft-polymerize the cationic monomer, 2-(dimethylamino)ethyl methacrylate (DMAEMA), to form side chains from the backbone. To stabilize the vehicle and also to decrease protein adsorption, oligo(ethylene glycol)methyl ether methacrylate (OEGMA) (M_n = 300 g/mol) was added as comonomer within the polymerization. As confirmed by ^{1}H NMR spectra (Figure S2), MBBs had ca. 65 wt % DMAEMA and ca. 35 wt % OEGMA (Table S1 for composition characterization). Importantly, the synthesis yielded three MBBs with varied AR from 1 to 4, denoted as AR1, AR2, and AR4. As confirmed by atomic force microscopy (AFM) (Figure 2a), the lengths of three samples (Figure 2d)

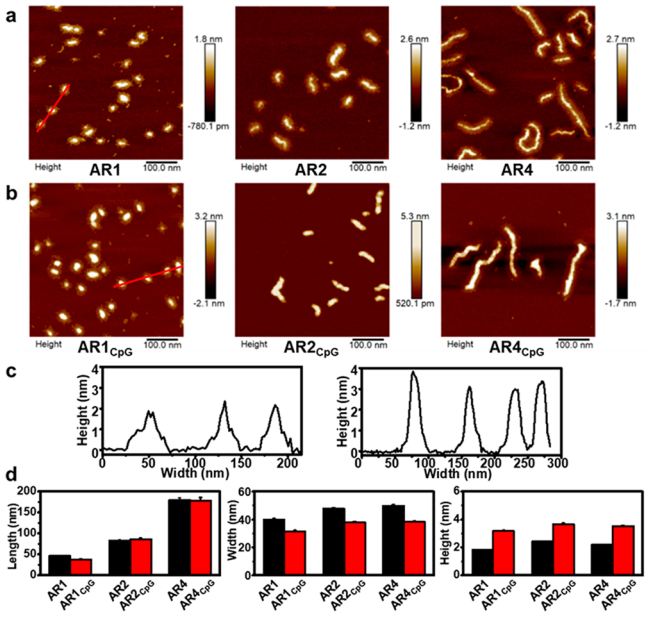

Figure 2. Characterization of MBB morphology with different AR. AFM images of (a) three parent MBBs and (b) their complexation with CpG. (c) Cross-section curves of AFM images (taking AR1 and $AR1_{CpG}$ as examples and corresponding to red lines in (a) and (b), respectively). (d) Statistic length, width and height of MBBs from AFM images. Data are expressed as mean ± SEM (n = 50).

were 46.7 ± 0.9 nm, 82.9 ± 2.7 nm, and 179.5 ± 5.4 nm, while their widths, 40.0 ± 0.7 nm, 47.8 ± 0.6 nm, and 49.8 ± 0.6 nm, respectively, were similar. Thus, prepared MBBs were readily soluble in water, while they retained sufficient positive charge for CpG loading.

Then, the MBB was incubated with CpG at various mass ratios, m_{MBB}/m_{CpG}, at a physiological pH. As seen in Figure S3, at mass ratio of 6, the disappearance of the free CpG band indicated a complete complexation between MBB and CpG. The content of loaded CpG could be evaluated to reach 14.3 wt %. Therefore, in the following assay, the mass ratio was fixed at 6 for all MBBs. Release of CpG in buffer was investigated at pH 7.4 and 5.0, showing stable CpG loading (Figure S4).

After CpG encapsulation, the morphology of nanoadjuvants, denoted as $AR1_{CpG}$, $AR2_{CpG}$, and $AR4_{CpG}$, was retained as shown by AFM in Figure 2b, and dynamic light scattering (DLS) results showed only minor changes in hydrodynamic diameters (Table S2). Relative to the MBBs before loading, the heights of nanoadjuvants increased obviously while the width became thinner, as shown by the cross-section curves of AFM images (Figure 2c). With $AR2_{CpG}$ as an example, the height increased from 2.4 to 3.7 nm, while the width decreased from 47.8 to 38.1 nm (Figure 2d). Such morphological deformation was attributed to the loading of CpG and polyplex formation reducing repulsion of cationic charges. It is noteworthy that the shapes of $AR2_{CpG}$ and $AR4_{CpG}$ were irregular wormlike, implying a semiflexible character.

To evaluate the stability of nanoadjuvants, DLS measurement was performed and a PBS buffer containing 50% of fetal bovine serum (FBS) was used to simulate a body fluid environment. The correlation function $g(t)_{mix}$ of $AR2_{CpG}$ could be fitted as intensity corrected combination of the individual correlation functions of $AR2_{CpG}$ in PBS, $g(t)_{AR2}$, and 50% of FBS, $g(t)_{FBS}$, indicating the absence of aggregation and also

https://doi.org/10.1021/acs.nanolett.1c02274
Nano Lett. 2021, 21, 7236−7243

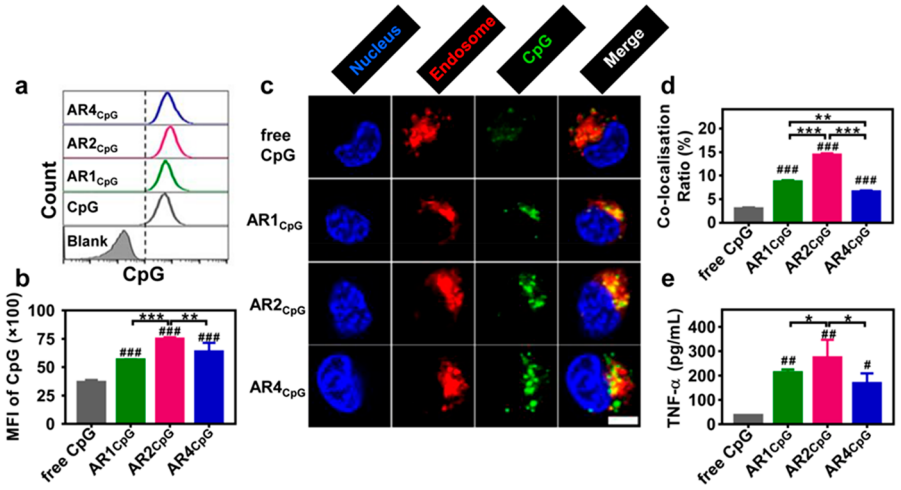

Figure 3. AR-dependent cellular uptake of nanoadjuvants. Cellular uptake of Cy5-labeled CpG was measured with flow cytometry, represented by (a) flow cytometry histograms and (b) corresponding mean fluorescence intensity (MFI) of CpG, after RAW264.7 cells were left untreated or treated with free CpG, $AR1_{CpG}$, $AR2_{CpG}$, or $AR4_{CpG}$ for 1 h at 37 °C. (c) RAW264.7 cells were observed by confocal microscopy, after incubation with free CpG, $AR1_{CpG}$, $AR2_{CpG}$, or $AR4_{CpG}$ for 1 h (CpG was labeled with Cy5). Cell nucleus was stained with Hoechst 33342 (blue) and the endosome was stained with lysotracker (red). Scale bar, 5 μm. (d) Quantitative colocalization ratio of Cy5-labeled CpG and endosomes was calculated by ImageJ software. (e) TNF-α expression were measured by ELISA after 12 h incubation of RAW264.7 with free CpG, $AR1_{CpG}$, $AR2_{CpG}$, or $AR4_{CpG}$. Data are expressed as mean ± SEM (n = 3 for b; n = 50 for d; n = 4 for e); *P < 0.05, **P < 0.01, ***P < 0.001 (significance levels among $AR1_{CpG}$, $AR2_{CpG}$, and $AR4_{CpG}$); #P < 0.05, ##P < 0.01, ###P < 0.001 (significance levels between free CpG and $AR1_{CpG}$, $AR2_{CpG}$, or $AR4_{CpG}$).

protein corona formation in biological environments[23] (Figure S5). It is important that the nanoadjuvants retained their size and morphology even in a biological media, which is critical for studying morphology effects on LN targeting without concerns of aggregation and protein corona.

Attributed to the introduction of OEGMA, zeta potentials of neat MBBs ranged from +10 to +11 mV (Table S2), much lower than the polyDMAEMA nanoparticles.[24] After loading with CpG, the nanoadjuvants underwent a further 1−2 mV decrease, but still maintained a slightly positive charge, which could facilitate uptake in antigen presenting cells (APCs). Cytotoxicity of MBB before and after CpG loading was evaluated with AR2 as an example. MTT assay after 48 h incubation showed that the IC_{50} of AR2 was larger than 100 μg/mL. The low cytotoxicity was likely attributable to the introduction of OEGMA in the hydrophilic shell of MBBs. When CpG was loaded, the sample became even less toxic, as cationic charges were compensated by CpG during complexation (Figure S6).

AR-Dependent Cellular Uptake and Activation of Nanoadjuvants. The shape of nanoparticles significantly influences nanoparticle−cell interactions that determine cellular uptake kinetic and mechanism.[13] First, three MBBs loaded with CpG were incubated with RAW264.7 cells (a mouse macrophage cell line), and free CpG was used as control. CpG was labeled with Cy5 (denoted as CpG-Cy5) for fluorescence quantitation. After 1 h incubation, the uptake ratio was determined by flow cytometry. As shown in Figure 3a,b, $AR2_{CpG}$ and $AR4_{CpG}$ exhibited a higher cell uptake compared with $AR1_{CpG}$ and free CpG. This result agrees with a former report that MBBs with an appropriate length, had a better cell internalization ability.[21] CpG is an agonist of TLR9, which is localized in the endosomal membrane, and thus, nanoadjuvants must be internalized in endosomes for efficient activation of APCs. Further studies were performed to evaluate the colocalization ratio of the nanoadjuvants and endosomes within RAW264.7 cells. Confocal images showed significantly higher colocalization with endosomes for all three MBBs carrying CpG compared with free CpG. It is noteworthy that, relative to $AR1_{CpG}$ and $AR4_{CpG}$, $AR2_{CpG}$ showed the highest level of colocalization (Figure 3c,d and Figure S7).

Accordingly, all three nanoadjuvants showed significantly higher stimulatory activity for RAW264.7 cells than free CpG. As seen in Figure 3e, nanoadjuvants induced much higher levels of TNF-α, a TLR9 activation indicator, compared with free CpG. Meanwhile, the MBBs also stimulated RAW264.7 cells to produce a low level of TNF-α (Figure S8), which is attributed to their low positive potential.[25,26] Interestingly, $AR2_{CpG}$ showed the best performance among the three nanoadjuvants. To evaluate whether these nanoadjuvants could increase the expression of costimulatory molecules on dendritic cells (DCs), bone marrow-derived DCs (BMDCs) were extracted from mice and stimulated with free CpG, $AR1_{CpG}$, $AR2_{CpG}$, or $AR4_{CpG}$. As shown in Figure S9, $AR2_{CpG}$ significantly increased expression of CD80 and CD86 costimulator and therefore promoted maturation of BMDCs. It was concluded from the above results that nanoadjuvants, especially $AR2_{CpG}$, remarkably enhanced the internalization of CpG by APCs, facilitated accumulation in endosomes, and thus promoted maturation of APCs, leading to pronounced cytokine production.

AR-Dependent LN Transportation and Localization in APCs of Nanoadjuvants. To amplify immune responses, it is necessary to deliver adjuvant and antigen to LNs.[3,27] To investigate transportation properties of nanoadjuvants to LNs, three samples loaded with CpG-Cy5 were injected in the footpad of mice, and free CpG-Cy5 was used as control. As seen in Figure S10, fluorescence signals at the injection site decreased over time. In contrast to free CpG, the MBBs loaded with CpG exhibited much longer retention time at the injection site. Mice were sacrificed at various time points after injection to isolate LNs for *ex vivo* imaging (Figure 4a).

https://doi.org/10.1021/acs.nanolett.1c02274
Nano Lett. 2021, 21, 7236−7243

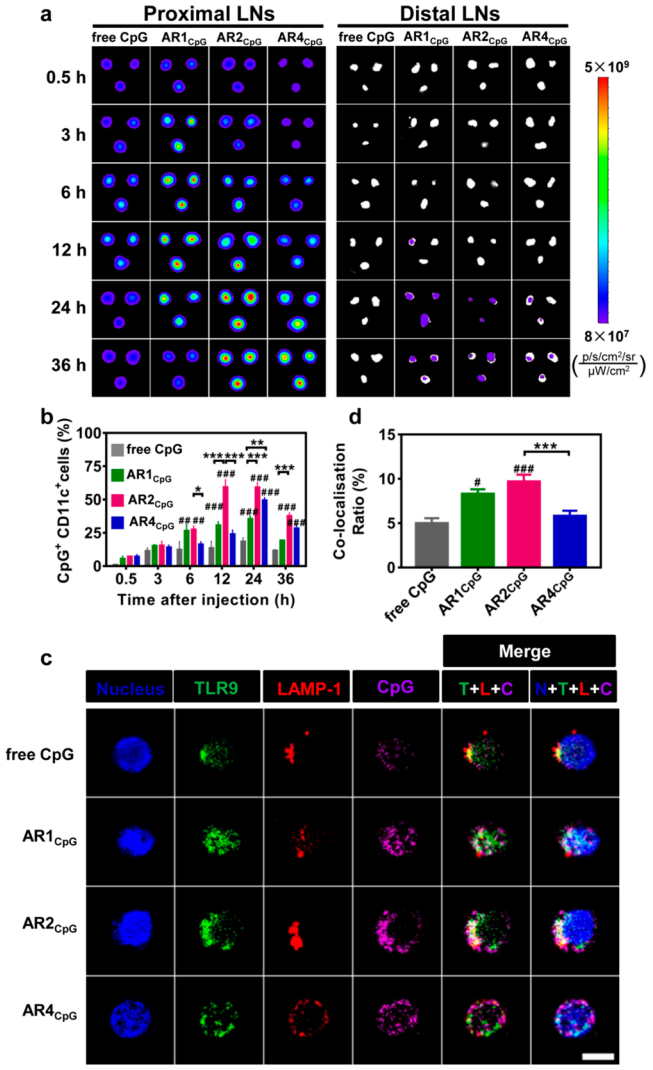

Figure 4. AR-dependent LN targeting transportation and *in vivo* uptake by LN-resident immune cells of nanoadjuvants. BALB/c mice were injected in the footpad with free CpG, $AR1_{CpG}$, $AR2_{CpG}$, or $AR4_{CpG}$ (CpG was labeled with Cy5). (a) Proximal (popliteal) and distal (inguinal) LNs were harvested and observed with IVIS imaging 0.5, 3, 6, 12, 24, and 36 h after injection. (b) Percentages of CpG^+ $CD11c^+$ cells in LNs are presented. Single cells in LNs were collected and analyzed for uptake of nanoadjuvants by flow cytometry. (c) Confocal images of $CD11c^+$ cells extracted from popliteal LNs. Popliteal LNs were harvested and $CD11c^+$ cells were isolated at 24 h after injection. The cell nucleus was stained with Hoechst 33342 (blue), TLR9 was stained using anti-TLR9-FITC (green), and LAMP-1 was stained using anti-LAMP1-Cy3 (red). In merged images, N, T, L, and C indicate nucleus, TLR9, LAMP-1, and CpG, respectively. Scale bar, 5 μm. (d) Quantitative colocalization ratio of CpG, TLR9, and LAMP-1 was calculated by ImageJ software. Data are expressed as mean ± SEM ($n = 4$ for b; $n = 15$ for c,d); $^*P < 0.05$, $^{**}P < 0.01$, $^{***}P < 0.001$ (significance levels among $AR1_{CpG}$, $AR2_{CpG}$, and $AR4_{CpG}$); $\#P < 0.05$, $\#\#\#P < 0.001$ (significance levels between free CpG and $AR1_{CpG}$, $AR2_{CpG}$, or $AR4_{CpG}$).

For proximal LNs, the fluorescence signal of free CpG peaked at 12 h, and then decayed. For $AR1_{CpG}$, the strongest signal also appeared at 12 h, but it is much stronger than that of free CpG, underlining the important role of nanovehicles. Noticeably, the maximum intensity for $AR2_{CpG}$ and $AR4_{CpG}$ was attained at 24 h and remained considerably high even at 36 h. Moreover, the CpG loaded in MBBs reached distal LNs at 24 h and showed retention (Figure 4a). From quantitative fluorescence intensity, among three nanoadjuvants, $AR2_{CpG}$ showed highest accumulation at draining LNs (Figure S11). To further prove nanoadjuvants draining to LNs, immunofluorescence staining for the tissue sections of LNs was implemented. It was found that $AR1_{CpG}$ and $AR2_{CpG}$ were presented in the subcapsular sinus of LNs 3 h post-injection. The fluorescence intensity of $AR2_{CpG}$ further increased 24 h post-injection, and $AR4_{CpG}$ also appeared in the subcapsular sinus (Figure S12).

Additionally, the fluorescence signals of MBB-loaded CpG were barely detected in heart, liver, spleen, lung, kidney, and serum, much lower than those of draining LNs, which indicated that the nanoadjuvants had excellent LN targeting properties (Figure S13a,b,c). More interestingly, though the signals in organs were very weak, free CpG was discernible in the kidney as early as 0.5 h, while the MBB-loaded CpG reached this site only from 6 h onward. At 24 h, no free CpG signal was observed in kidney, while MBB-loaded CpG remained apparent until 36 h (Figure S13a,b), indicating sustaining release of CpG in the lymphatic system. These results were consistent with the retention results at injection sites (Figure S10). Together with the results in LNs, the data indicated that MBBs showed unique kinetics distribution *in vivo* and delayed expulsion from the kidney. Among the three nanoadjuvants, the kinetics of LN targeting, major organ distribution, and injection site retention were dependent on AR, which was remarkable.

In the above experiments, the nanoadjuvants showed distinguishable LN targeting in mice. However, amplified immunity is dependent on whether the CpG carried by MBBs can be delivered to its receptor, TLR9. Next, we investigated the uptake of nanoadjuvants by lymph node-resident immune cells *in vivo*. At the indicated time after injection, cells from draining LNs were extracted, labeled, and analyzed by flow cytometry. As shown in Figure 4b and Figure S14, the uptake of CpG in $AR1_{CpG}$ and $AR2_{CpG}$ groups by $CD11c^+$ cells (APCs subsets) in LNs started to increase at 6 h after injection, compared with free CpG and $AR4_{CpG}$. At 12 h, internalization of $AR2_{CpG}$ by $CD11c^+$ in LNs increased much more significantly. The steady increase of $AR2_{CpG}$ remained observable at 24 h. More than 50% of $CD11c^+$ cells in the proximal LNs endocytosed $AR2_{CpG}$ at these two time points. For $AR4_{CpG}$, the increased uptake by $CD11c^+$ cells in LNs started slowly but also reached a maximum at 24 h, and was only slightly lower than that for $AR2_{CpG}$. Both $AR2_{CpG}$ and $AR4_{CpG}$ signals substantially decreased at 36 h.

Upon uptake into APCs and transport to the endosome, TLR9 is only effectively activated when CpG reaches an endosomal compartment and thus can induce a potent immune response.[28] Thus, we further investigated whether the CpG carried by MBBs colocalized with TLR9 in the late endosome *in vivo*. $CD11c^+$ cells from proximal LNs were isolated at 24 h after injection. The confocal microscopy images displayed strong colocalization of $AR2_{CpG}$, TLR9, and lysosome-associated membrane protein 1 (LAMP1), a standard marker for late endosomal compartments. Co-localization was obviously stronger than that of free CpG or any other nanoadjuvant (Figure 4c, d). Therefore, a defined AR of 1D nanoadjuvants may ensure optimum colocalization between delivered adjuvants and TLR9 in APCs *in vivo*.

AR-Dependent Immunotherapy of Nanoadjuvants in a Mouse Model of CHB. Encouraged by the above results,

https://doi.org/10.1021/acs.nanolett.1c02274
Nano Lett. 2021, 21, 7236−7243

we next studied the therapeutic role of nanoadjuvants in HBV-infected mice with respect to AR dependence. A universally accepted murine model was adopted, using tail intravenous injection of rAAV-1.3HBV (Figure 5a left), which partially

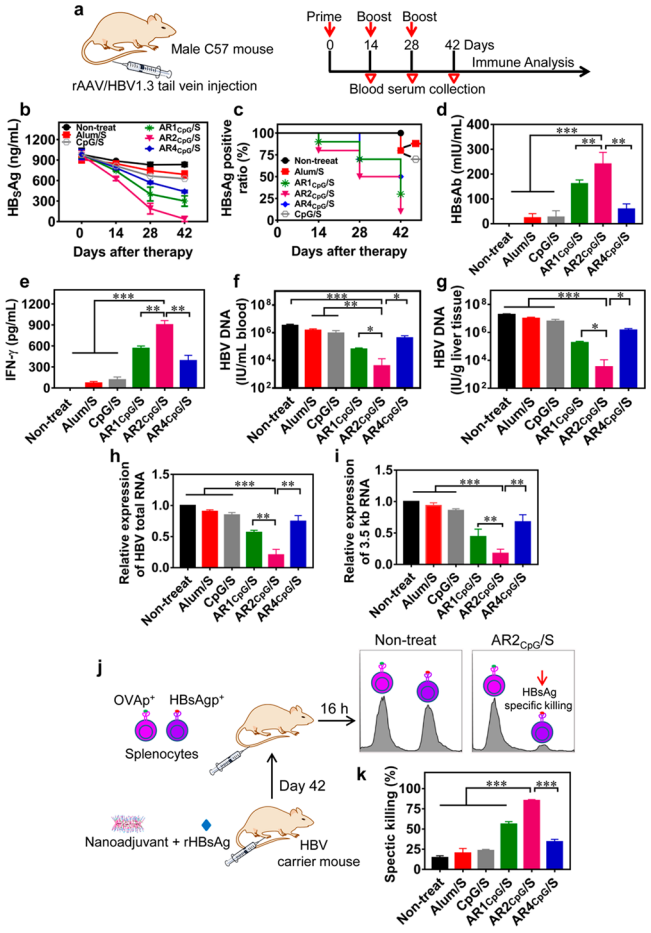

Figure 5. AR-dependent HBV elimination of nanoadjuvants in HBV carrier mice. (a) Schematic illustration of establishing HBV-carrier mouse and the schedule of immune analysis. (b) HBsAg, (d) HBsAb, and (e) IFN-γ levels in the blood were detected after different formulation therapy. (c) HBsAg positive ratio of HBV carrier mice was evaluated after different formulation therapy. HBV DNA levels in (f) blood and (g) liver of HBV carrier mice were detected with q-PCR on day 42 after different formulations therapy. Expression of (h) HBV total RNA and (i) HBV 3.5 kb RNA in liver of HBV-carrier mice were detected with q-PCR on day 42 after different formulation therapy. (j) Schematic illustration of the *in vivo* CTL lysis assay for proving the functional recovery of T cells in treated-HBV carrier mice. (k) Quantitative comparison of HBsAg-specific CTL response in treated-HBV carrier mice with different formulations. Data are expressed as mean ± SEM (n = 5 for b, d, e, f, g, h, i; n = 10 for c; n = 3 for j, k); *P < 0.05, **P < 0.01, ***P < 0.001.

mimics the immunological characteristics of CHB.[29] HBV-carrier mice were treated subcutaneously with different nanoadjuvants in combination with rHBsAg (denoted as $AR1_{CpG}$/S, $AR2_{CpG}$/S, and $AR4_{CpG}$/S; S represents rHBsAg). Free CpG and alum adjuvant with rHBsAg as control (denoted as CpG/S and Alum/S), the time schedule was given in Figure 5a (right).

The mice were bled fortnightly to monitor levels of serum HBsAg, anti-HBsAg antibody (HBsAb), and IFN-γ with quantitative ELISA. For CpG/S and Alum/S, on day 42, serum HBsAg in carrier mice showed only a slight decline compared with the nontreatment group, in line with previous observations.[30] In contrast, all three nanoadjuvant groups demonstrated tremendous decreases in serum HBsAg levels in vaccinated mice with increasing treatment time (Figure 5b). Moreover, $AR2_{CpG}$/S immunization almost completely cleared HBsAg from the serum. The response ratio in HBV-carrier mice remarkably increased in nanoadjuvant-treated groups. Most importantly, 90% of infected mice achieved HBsAg seroclearance, an important marker for clinical cure of chronic HBV infection,[31] in the $AR2_{CpG}$/S group on day 42 (Figure 5c). After treatment, the production of HBsAb was significantly increased in all nanoadjuvant groups, but once again $AR2_{CpG}$/S performed the best (Figure 5d). In contrast, serum HBsAb remained at barely detectable levels in the CpG/S and Alum/S groups. IFN-γ, a cytokine reflecting cellular immunity that plays a pivotal role in antiviral activities in HBV-related diseases, displayed a similar response behavior. For all nanoadjuvants, elevated IFN-γ levels were detected on day 42, while IFN-γ levels remained low in the CpG/S and Alum/S group. Among the nanoadjuvants, the $AR2_{CpG}$/S group again showed the best performance (Figure 5e).

Next, the effect of nanoadjuvants for HBV therapy at the gene level was evaluated with quantitative PCR. HBV is a hepatotropic virus; after infection and replication in hepatocytes, it enters the blood.[32,33] HBV DNA levels in blood were investigated in HBV-infected mice (Figure 5f). A remarkable decline on day 42 in all nanoadjuvant-treated groups was observed, which was 1−2 orders of magnitude lower than HBV DNA levels in the CpG/S and Alum/S groups. Notably, carrier mice in the $AR2_{CpG}$/S group showed the lowest HBV DNA levels in blood, which were more than 100 times reduced compared with nontreated, CpG/S, and Alum/S treated mice.

Whether HBV in hepatocytes is cleared or not determines the therapeutic outcome of CHB. As shown in Figure 5g, HBV DNA in livers of carrier mice treated with $AR2_{CpG}$/S also showed lowest levels on day 42. Simultaneously, inhibition of HBV DNA transcription in the liver after treatment was also detected at RNA level on day 42. The expression of HBV total RNA in the livers of infected mice treated with $AR2_{CpG}$/S was obviously inhibited compared with the other groups (Figure 5h). HBV 3.5 kb RNA is closely related to the formation of HBV cccDNA,[34,35] and the expression of this in the liver of infected mice treated with $AR2_{CpG}$/S was also substantially reduced after treatment (Figure 5i). The reduction of HBV DNA and RNA in hepatocytes of the $AR2_{CpG}$/S group was evidently the reason for the nearly complete clearance of serum HBsAg.

An *in vivo* cytotoxic T lymphocyte (CTL) lysis assay was implemented to prove the functional recovery of T-cells in HBV-infected mice.[36] Briefly, splenocytes from normal mice were divided into two groups. One group was incubated with HBsAg-derived peptide ($HBsAgp^+$) and the other was incubated with OVA-derived peptide ($OVAp^+$). They were then respectively labeled with high and low concentrations of carboxy fluorescein succinimidyl ester (CFSE) and mixed at an equal quantitative ratio, followed by adoptive transfer into the treated HBV-infected mice on day 42 (Figure 5j). Sixteen hours later, the nanoadjuvants induced a dramatically enhanced HBsAg-specific CTL response, in which the $AR2_{CpG}$/S group cleared 85% of $HBsAgp^+$ splenocytes (Figure 5k). This result indicated that the nanoadjuvants restored T-

https://doi.org/10.1021/acs.nanolett.1c02274
Nano Lett. 2021, 21, 7236−7243

cell function and elicited a strong anti-HBsAg response in HBV-infected mice.

The elimination of HBV-infected hepatocytes is a key indicator for CHB cure.[36] Thus, we stained liver sections from infected mice with anti-HBsAg and anti-HBcAg antibodies on day 42 (Figure S15). The number of HBsAg-positive and HBcAg-positive hepatocytes dramatically decreased in HBV-carrier mice treated with nanoadjuvants. In the $AR2_{CpG}$/S group, hardly any positive cells were detected. In contrast, HBsAg-positive and HBcAg-positive hepatocytes remained strongly detectable in sections from the CpG/S, Alum/S, and untreated groups. Therefore, nanoadjuvants restored B-cell and T-cell response against HBV, breaking immune tolerance, and ultimately resulting in HBsAb seroconversion and HBsAg clearance in HBV-infected mice.

CONCLUSION

In the past decade, 1D particles have attracted much attention in nanomedicine to interpret the influence of nanoparticle shape on functions. Unfortunately, choices for a 1D materials toolbox with rational designability for a clear understanding of parameters and properties remain rare. Here, we chose MBB, a unimolecular nanoparticle, for LN targeted delivery of molecular adjuvants because its AR and structure can be rationally designed and precisely prepared at a scale of <100 nm, which is required for targeting LN-resident DCs. Moreover, MBBs have a persistent length on tens of nanometers in general,[22] showing a semiflexible conformation. This characteristic may allow the morphology of 1D nanoparticles to be adapted to overcome biological barriers in extravasation and penetration of the ECM in LNs.

Among the three nanoadjuvants, $AR2_{CpG}$ exhibited the best cellular uptake by RAW264.7 macrophages *in vitro*. However, it could be difficult to elucidate performance *in vivo* using known model pathways because many factors are involved. Thus, we isolated LN-resident DCs from injected mice and confirmed a higher level of $AR2_{CpG}$ in the APCs of proximal LNs among three samples. Moreover, $AR2_{CpG}$ showed stronger colocalization with late endosomes than the other two nanoadjuvants. This finding is particularly important because late endosomes are the compartments where TLR9 is located in primary APCs for CpG-induced activation. This unique behavior leads to higher levels of TNF-α, costimulatory molecules CD80 and CD86, and thus promotes more efficient maturation of DCs. It is interesting that the longer $AR4_{CpG}$ did not outperform the shorter $AR2_{CpG}$. This is understandable because, though its diameter is the same as that of the shorter MBB, the longer nanoadjuvant has a larger hydrodynamic radius, which may not benefit transportation, extravasation, and diffusion in LNs. However, $AR2_{CpG}$ with an optimum AR may demonstrate preferential traffic kinetics and better cellular endocytosis *in vivo*.

CHB is a serious liver infection caused by HBV. Although great research has been invested in developing HBV therapeutic vaccines to eradicate HBV,[37,38] these vaccines failed because of using conventional adjuvants.[39] Since nanoparticles may interact more effectively with APCs,[40] our immunization with defined nanoadjuvants demonstrate a significant decrease of HBV infection-related markers while increasing production of HBsAb and IFN-γ, as markers of the desired immune response. Among three adjuvants, $AR2_{CpG}$ with rHBsAg achieved the most efficient clearance of HBV, attributed to its better performance in targeting LN-resident DCs and cellular colocalization to enhance antigen immunogenicity.

Our data indicate that 1D nanoadjuvants with the correct AR can be efficiently targeted to LNs, reach DCs and colocalize with late endosomes, leading to potent immune responses against the HBV to successfully cure CHB. This research will stimulate development of potent vaccines to combat persistent diseases by using powerful new adjuvants.

ASSOCIATED CONTENT

Supporting Information

The Supporting Information is available free of charge at https://pubs.acs.org/doi/10.1021/acs.nanolett.1c02274.

Detailed chemical composition, diameter and zeta potential of cationic MBBs, gel electrophoresis assay, *in vitro* release profile and DLS results of nanoadjuvants, cytotoxicity, cellular activation, as well as biodistribution study of nanoadjuvants (PDF)

AUTHOR INFORMATION

Corresponding Authors

Lixin Liu − *School of Materials Science and Engineering, Key Laboratory for Polymeric Composite and Functional Materials of Ministry of Education, Sun Yat-sen University, Guangzhou 510275, China; State Key Laboratory of Oncology in Southern China, Sun Yat-sen University Cancer Center, Guangzhou 510060, China;* orcid.org/0000-0001-6133-4977; Email: liulixin@mail.sysu.edu.cn

Yongming Chen − *School of Materials Science and Engineering, Key Laboratory for Polymeric Composite and Functional Materials of Ministry of Education, Sun Yat-sen University, Guangzhou 510275, China; State Key Laboratory of Oncology in Southern China, Sun Yat-sen University Cancer Center, Guangzhou 510060, China;* orcid.org/0000-0003-2843-5543; Email: chenym35@mail.sysu.edu.cn

Authors

Ziyang Sun − *School of Materials Science and Engineering, Key Laboratory for Polymeric Composite and Functional Materials of Ministry of Education, Sun Yat-sen University, Guangzhou 510275, China*

Dongdong Qiao − *School of Materials Science and Engineering, Key Laboratory for Polymeric Composite and Functional Materials of Ministry of Education, Sun Yat-sen University, Guangzhou 510275, China*

Yi Shi − *School of Materials Science and Engineering, Key Laboratory for Polymeric Composite and Functional Materials of Ministry of Education, Sun Yat-sen University, Guangzhou 510275, China;* orcid.org/0000-0003-2943-5465

Matthias Barz − *Leiden Academic Center for Drug Research, Division of Biotherapeutics, Laboratory for Biotherapeutic Delivery, Leiden University, 2333 CC Leiden, The Netherlands; Department Chemie, Johannes Gutenberg University, 55099 Mainz, Germany;* orcid.org/0000-0002-1749-9034

Complete contact information is available at: https://pubs.acs.org/10.1021/acs.nanolett.1c02274

https://doi.org/10.1021/acs.nanolett.1c02274
Nano Lett. 2021, 21, 7236−7243

Author Contributions

Z.S. and D.Q. contributed equally to the work; Z.S. conducted chemistry and physical characterization; D.Q. conducted biological part; Y.S. supervised chemistry; M.B. supplied discussion; L.L. supervised the biological study; Y.M. supervised and wrote manuscript.

Notes

The authors declare no competing financial interest.

■ ACKNOWLEDGMENTS

This work was supported by National Natural Science Foundation of China (22075324, 51533009) and the Key Areas Research and Development Program of Guangzhou (202007020006).

■ REFERENCES

(1) Reed, S. G.; Orr, M. T.; Fox, C. B. Key roles of adjuvants in modern vaccines. *Nat. Med.* **2013**, *19*, 1597−1608.
(2) Coffman, R. L.; Sher, A.; Seder, R. A. Vaccine adjuvants: putting innate immunity to work. *Immunity* **2010**, *33*, 492−503.
(3) Schudel, A.; Francis, D. M.; Thomas, S. N. Material design for lymph node drug delivery. *Nat. Rev. Mater.* **2019**, *4*, 415−428.
(4) Sainte-Marie, G. The lymph node revisited: development, morphology, functioning, and role in triggering primary immune responses. *Anat. Rec.* **2010**, *293*, 320−337.
(5) Mancini, R. J.; Stutts, L.; Ryu, K. A.; Tom, J. K.; Esser-Kahn, A. P. Directing the immune system with chemical compounds. *ACS Chem. Biol.* **2014**, *9*, 1075−1085.
(6) Krieg, A. M. CpG motifs in bacterial DNA and their immune effects. *Annu. Rev. Immunol.* **2002**, *20*, 709−760.
(7) Bonavida, B. Immunomodulatory effect of tumor necrosis factor. *Biotherapy* **1991**, *3*, 127−133.
(8) Gupta, A.; Das, S.; Schanen, B.; Seal, S. Adjuvants in micro- to nanoscale: current state and future direction. *Wiley Interdiscip. Rev.: Nanomed. Nanobiotechnol.* **2016**, *8*, 61−84.
(9) Li, X.; Wang, X.; Ito, A. Tailoring inorganic nanoadjuvants towards next-generation vaccines. *Chem. Soc. Rev.* **2018**, *47*, 4954−4980.
(10) Williams, D. S.; Pijpers, I. A. B.; Ridolfo, R.; van Hest, J. C. M. Controlling the morphology of copolymeric vectors for next generation nanomedicine. *J. Controlled Release* **2017**, *259*, 29−39.
(11) Reddy, S. T.; van der Vlies, A. J.; Simeoni, E.; Angeli, V.; Randolph, G. J.; O'Neil, C. P.; Lee, L. K.; Swartz, M. A.; Hubbell, J. A. Exploiting lymphatic transport and complement activation in nanoparticle vaccines. *Nat. Biotechnol.* **2007**, *25*, 1159−1164.
(12) Manolova, V.; Flace, A.; Bauer, M.; Schwarz, K.; Saudan, P.; Bachmann, M. F. Nanoparticles target distinct dendritic cell populations according to their size. *Eur. J. Immunol.* **2008**, *38*, 1404−13.
(13) Kinnear, C.; Moore, T. L.; Rodriguez-Lorenzo, L.; Rothen-Rutishauser, B.; Petri-Fink, A. Form follows function: nanoparticle shape and its implications for nanomedicine. *Chem. Rev.* **2017**, *117*, 11476−11521.
(14) Mhatre, O.; Sodha, S. Pharmaceutical feasibility and flow characteristics of polymeric non-spherical particles. *Nanomedicine* **2019**, *18*, 243−258.
(15) Hassan, H. A. F. M.; Smyth, L.; Rubio, N.; Ratnasothy, K.; Wang, J. T. W.; Bansal, S. S.; Summers, H. D.; Diebold, S. S.; Lombardi, G.; Al-Jamal, K. T. Carbon nanotubes' surface chemistry determines their potency as vaccine nanocarriers in vitro and in vivo. *J. Controlled Release* **2016**, *225*, 205−216.
(16) Sun, B. B.; Ji, Z. X.; Liao, Y. P.; Chang, C. H.; Wang, X.; Ku, J.; Xue, C. Y.; Mirshafiee, V.; Xia, T. Enhanced immune adjuvant activity of aluminum oxyhydroxide nanorods through cationic surface functionalization. *ACS Appl. Mater. Interfaces* **2017**, *9*, 21697−21705.
(17) Kumar, S.; Anselmo, A. C.; Banerjee, A.; Zakrewsky, M.; Mitragotri, S. Shape and size-dependent immune response to antigen-carrying nanoparticles. *J. Controlled Release* **2015**, *220*, 141−148.
(18) Meyer, R. A.; Sunshine, J. C.; Perica, K.; Kosmides, A. K.; Aje, K.; Schneck, J. P.; Green, J. J. Biodegradable nanoellipsoidal artificial antigen presenting cells for antigen specific T-cell activation. *Small* **2015**, *11*, 1519−1525.
(19) Chen, Y. M. Shaped hairy polymer nanoobjects. *Macromolecules* **2012**, *45*, 2619−2631.
(20) Sun, Z.Y.; Li, H.A.; Huang, H.H.; Shi, Y.; Chen, Y.M. The applications of molecular bottlebrush in nanomedicine. *Acta Polym. Sin.* **2020**, *51*, 609−619.
(21) Li, H. A.; Liu, H.; Nie, T. Q.; Chen, Y.; Wang, Z. Y.; Huang, H. H.; Liu, L. X.; Chen, Y. M. Molecular bottlebrush as a unimolecular vehicle with tunable shape for photothermal cancer therapy. *Biomaterials* **2018**, *178*, 620−629.
(22) Gerle, M.; Fischer, K.; Roos, S.; Muller, A. H. E.; Schmidt, M.; Sheiko, S. S.; Prokhorova, S.; Moller, M. Main chain conformation and anomalous elution behavior of cylindrical brushes as revealed by GPC/MALLS, light scattering, and SFM. *Macromolecules* **1999**, *32*, 2629−2637.
(23) Rausch, K.; Reuter, A.; Fischer, K.; Schmidt, M. Evaluation of nanoparticle aggregation in human blood serum. *Biomacromolecules* **2010**, *11*, 2836−2839.
(24) Krishnamoorthy, M.; Li, D.; Sharili, A. S.; Gulin-Sarfraz, T.; Rosenholm, J. M.; Gautrot, J. E. Solution conformation of polymer brushes determines their interactions with DNA and transfection efficiency. *Biomacromolecules* **2017**, *18*, 4121−4132.
(25) Luo, M.; Wang, H.; Wang, Z.; Cai, H.; Lu, Z.; Li, Y.; Du, M.; Huang, G.; Wang, C.; Chen, X.; Porembka, M. R.; Lea, J.; Frankel, A. E.; Fu, Y.; Chen, Z. J.; Gao, J. A. STING-activating nanovaccine for cancer immunotherapy. *Nat. Nanotechnol.* **2017**, *12*, 648−654.
(26) Yang, W.; Zhu, G.; Wang, S.; Yu, G.; Yang, Z.; Lin, L.; Zhou, Z.; Liu, Y.; Dai, Y.; Zhang, F.; Shen, Z.; Liu, Y.; He, Z.; Lau, J.; Niu, G.; Kiesewetter, D. O.; Hu, S.; Chen, X. *In Situ* dendritic cell vaccine for effective cancer immunotherapy. *ACS Nano* **2019**, *13*, 3083−3094.
(27) Jiang, H.; Wang, Q.; Sun, X. Lymph node targeting strategies to improve vaccination efficacy. *J. Controlled Release* **2017**, *267*, 47−56.
(28) de Jong, S. D.; Basha, G.; Wilson, K. D.; Kazem, M.; Cullis, P.; Jefferies, W.; Tam, Y. The immunostimulatory activity of unmethylated and methylated CpG oligodeoxynucleotide is dependent on their ability to colocalize with TLR9 in late endosomes. *J. Immunol.* **2010**, *184*, 6092−6102.
(29) Yang, D.; Liu, L.; Zhu, D.; Peng, H.; Su, L.; Fu, Y. X.; Zhang, L. A mouse model for HBV immunotolerance and immunotherapy. *Cell. Mol. Immunol.* **2014**, *11*, 71−78.
(30) Dienstag, J. L.; Stevens, C. E.; Bhan, A. K.; Szmuness, W. Hepatitis B vaccine administered to chronic carriers of hepatitis B surface antigen. *Ann. Intern. Med.* **1982**, *96*, 575−579.
(31) Trepo, C.; Chan, H. L. Y.; Lok, A. Hepatitis B virus infection. *Lancet* **2014**, *384*, 2053−2063.
(32) Seto, W. K.; Lo, Y. R.; Pawlotsky, J. M.; Yuen, M. F. Chronic hepatitis B virus infection. *Lancet* **2018**, *392*, 2313−2324.
(33) Yuen, M. F.; Chen, D. S.; Dusheiko, G. M.; Janssen, H. L. A.; Lau, D. T. Y.; Locarnini, S. A.; Peters, M. G.; Lai, C. L. Hepatitis B virus infection. *Nat. Rev. Dis. Primers* **2018**, *4*, 20.
(34) Tang, H.; Banks, K. E.; Anderson, A. L.; McLachlan, A. Hepatitis B virus transcription and replication. *Drug News Perspect* **2001**, *14*, 325−334.
(35) Oropeza, C. E.; Tarnow, G.; Sridhar, A.; Taha, T. Y.; Shalaby, R. E.; McLachlan, A. The regulation of HBV transcription and replication. *Adv. Exp. Med. Biol.* **2020**, *1179*, 39−69.
(36) Wang, X. Z.; Dong, A. H.; Xiao, J. J.; Zhou, X. J.; Mi, H. L.; Xu, H. Q.; Zhang, J. M.; Wang, B. Overcoming HBV immune tolerance to eliminate HBsAg-positive hepatocytes via pre-administration of GM-CSF as a novel adjuvant for a hepatitis B vaccine in HBV transgenic mice. *Cell. Mol. Immunol.* **2016**, *13*, 850−861.
(37) Kosinska, A. D.; Bauer, T.; Protzer, U. Therapeutic vaccination for chronic hepatitis B. *Curr. Opin. Virol.* **2017**, *23*, 75−81.

https://doi.org/10.1021/acs.nanolett.1c02274
Nano Lett. 2021, 21, 7236−7243

(38) Li, J.; Bao, M.; Ge, J.; Ren, S.; Zhou, T.; Qi, F.; Pu, X.; Dou, J. Research progress of therapeutic vaccines for treating chronic hepatitis B. *Hum. Vaccines Immunother.* **2017**, *13*, 986−997.
(39) Bian, G.; Cheng, Y.; Wang, Z.; Hu, Y.; Zhang, X.; Wu, M.; Chen, Z.; Shi, B.; Sun, S.; Shen, Y.; Chen, E. j.; Yao, X.; Wen, Y.; Yuan, Z. Whole recombinant Hansenula polymorpha expressing hepatitis B virus surface antigen (yeast-HBsAg) induces potent HBsAg-specific Th1 and Th2 immune responses. *Vaccine* **2009**, *28*, 187−194.
(40) Ke, X.; Howard, G. P.; Tang, H.; Cheng, B.; Saung, M. T.; Santos, J. L.; Mao, H. Q. Physical and chemical profiles of nanoparticles for lymphatic targeting. *Adv. Drug Delivery Rev.* **2019**, *151−152*, 72−93.

https://doi.org/10.1021/acs.nanolett.1c02274
Nano Lett. 2021, 21, 7236−7243